The Astrophysical Journal, 951:57 (12pp), 2023 July 1 https://doi.org/10.3847/1538-4357/acd0ad

Doppler Broadening and Line-of-sight Effects in Core-collapse Supernovae and Young Remnants

Taylor Jacovich[1,2,3], Daniel Patnaude[1], Patrick Slane[1], Carles Badenes[4], Shiu-Hang Lee[5,6], Shigehiro Nagataki[7], and Dan Milisavljevic[8]
[1] Center for Astrophysics | Harvard & Smithsonian, 60 Garden Street, Cambridge, MA 02138, USA; tjacovich@cfa.harvard.edu
[2] The George Washington University, Department of Physics, 725 21st Street NW, Washington, DC 20052, USA
[3] Astronomy, Physics, and Statistics Institute of Sciences (APSIS), 725 21st Street NW, Washington, DC 20052, USA
[4] Department of Physics and Astronomy and Pittsburgh Particle Physics Astrophysics and Cosmology Center (PITT PACC), University of Pittsburgh, 3941 O'Hara Street, Pittsburgh, PA 15260, USA
[5] Department of Astronomy, Kyoto University Oiwake-cho, Kitashirakawa, Sakyo-ku, Kyoto 606-8502, Japan
[6] Kavli Institute for the Physics and Mathematics of the Universe (WPI), The University of Tokyo, Kashiwa 277-8583, Japan
[7] RIKEN 2-1 Hirosawa, Wako, Saitama 351-0198, Japan
[8] Department of Physics and Astronomy, Purdue University, 525 Northwestern Avenue, West Lafayette, IN 47907, USA

Received 2021 September 9; revised 2023 April 25; accepted 2023 April 25; published 2023 July 3

Abstract

The dynamics and spectral characteristics of supernova ejecta reveal details of the supernova energetics, explosive nucleosynthesis, and evolution of the progenitor. However, in practice, this important diagnostic information is only derived from CCD-resolution X-ray spectra of shock-heated material. If the spectra were to be observed at higher resolution, then important clues to the explosion energetics would be obvious through measurements of bulk Doppler motions and turbulence in the ejecta. Likewise, the unshocked ejecta in supernovae and young remnants are responsible for obscuring the emission from ejecta on the back side of the remnant. In light of these important effects, we present line-of-sight spectral maps of core-collapse supernova remnant models. We explore the bulk Doppler broadening of spectral lines, including line-of-sight effects. We also explore the time-dependent absorption from both shocked and unshocked ejecta. Finally, we discuss how future X-ray missions such as XRISM and Athena will be able to resolve these effects in nearby and extragalactic supernovae and their remnants.

Unified Astronomy Thesaurus concepts: Supernova remnants (1667); Core-collapse supernovae (304); Astronomical simulations (1857); Computational methods (1965); X-ray observatories (1819)

1. Introduction

Core-collapse supernovae (CCSNe) and their remnants are integral in driving galactic chemical evolution, star formation, and the formation of compact objects such as neutron stars (NSs) and black holes. Observations of Galactic supernova remnants (SNRs) provide important insights into the formation of intermediate-mass and Fe-group elements, but these objects are often observed through a veil of interstellar neutral hydrogen that obscures all but the coolest and hottest material. Additionally, due to the problem of Galactic interstellar absorption, the observed population of SNRs is likely incomplete. Regardless, spatially resolved studies of these objects allow us to probe the energetics of the explosion mechanism, which is encoded not only in the chemistry of the ejecta but also in the bulk velocity of the material. Dispersive X-ray and optical spectroscopy can measure the radial velocity of the material, allowing for a 3D reconstruction of the ejecta, which contains an imprint of the explosion (Flanagan et al. 2004; DeLaney et al. 2010; Milisavljevic & Fesen 2013).

In contrast, surveying external galaxies allows us to reconstruct the complete population of SNRs (e.g., M51; Winkler et al. 2021), but often at the expense of spatial resolution ($1'' \approx 50$ pc at 10 Mpc). Still, the integrated spectra, particularly at optical wavelengths where such measurements are accessible, reveal a great deal about the bulk motion of the ejecta (Milisavljevic et al. 2012; Quirola-Vásquez et al. 2019), and, when taken at high cadence (e.g., SN 1987A, SN 1979C, SN 1986J, SNR 4449-1; Milisavljevic & Fesen 2008; Milisavljevic et al. 2008, 2009; Fransson et al. 2013), directly probe different layers of the ejecta and allow us to examine the poorly understood transition from supernova (SN) to SNR (Milisavljevic & Fesen 2017; Ramakrishnan & Dwarkadas 2020). Existing high-resolution X-ray spectroscopy of a few objects (notably, SN 1987A and SN 1996cr and Type Ia objects like Tycho) already informs us on both the composition and bulk dynamics of the ejecta and can also probe the unshocked component by looking at absorption of X-rays emitted from the back side of the remnant (Sato & Hughes 2017; Alp et al. 2018). Planned missions, such as the Athena X-IFU, will perform nondispersive spectroscopy at $5''$ scales (Barret et al. 2016), allowing for detailed studies of a larger number of young remnants. The XRISM will have similar spectral resolution and a larger effective area around ∼6 keV at angular scales closer to $1\overset{\prime}{.}7$ (XRISM Science Team 2020).

Here we extend the grid of CCSN remnant models presented in Jacovich et al. (2021, hereafter Paper I). We focus on the effects of Doppler broadening and absorption by shocked and unshocked material and the effect these have on the integrated X-ray spectrum. We start with progenitor and remnant models presented in Paper I and, using the dynamics and chemical composition of the ejecta, compute the optical depth of the shocked and unshocked material as a function time. We then use the optical depth to calculate the line-of-sight (LOS) X-ray spectrum, including the effects of both Doppler broadening and intrinsic absorption, in Section 2. We examine the complexity the Doppler broadening introduces to the spectrum in Section 3.1 and close with a discussion about the observability of these models and features with future X-ray missions in Section 3.2.

2. Methods

Remnant models are constructed using a multistage pipeline simulating the entire remnant life cycle from pre-main-sequence progenitor through core collapse and into the remnant phase. Some important aspects of the models are covered below, but the full description of the pipeline and the details of the progenitor objects can be found in Paper I. To study the LOS effects, we examined the remnants of single star models with wind-driven mass loss. These models covered the IIP, IIL, and IIb progenitor types and were assumed to be in a circumstellar medium (CSM) that reflected a red supergiant wind. The remnant phase is handled by the cosmic-ray hydrodynamics code `ChN`, which simulates the remnant dynamics based on an initial progenitor model and couples the dynamical simulation to a full nonequilibrium ionization calculation to define the ionization state of the remnant. Cosmic-ray acceleration can also be simulated, but we choose to operate in the test particle limit for the current set of models (Patnaude et al. 2009, 2010; Lee et al. 2014).

In general, remnant spectra consist of a few key emission components that emerge from the underlying system. The largest contributors are continuum components with emission from nonthermal sources such as synchrotron emission and thermal sources such as thermal bremsstrahlung, with atomic line emission complexes contributing in varying degrees, depending on the ionization state of the remnant (e.g., Vink 2012, and references therein). The continuum can be used as a probe of the plasma state of the remnant and provides a measure of the electron temperature. The atomic line emission can give a more detailed description of the composition of the remnant, ionization state, and ion heating (Porquet et al. 2001). We further expand on the utility of atomic line emission by using it as a probe of intraremnant absorption, as well as Doppler broadening from remnant expansion.

2.1. Spectra Extraction and Absorption from LOS Ray-tracing

Spectra are computed by passing the ionization information to a thermal emission code coupled to `atomdb` (Foster et al. 2017) and are computed for each emitting cell in the simulation based on the local fluid and ionization conditions of the cell. By assuming the cell is a uniformly emitting region, we can calculate the specific flux for each cell as

$$f(\nu) = \frac{F(\nu)_{\mathrm{cell}}}{V_{\mathrm{cell}}}. \tag{1}$$

The true observed flux of each cell is thus

$$F_{\mathrm{obs}}^{\mathrm{cell}} = f(\nu) A_{\mathrm{cell}} l_{\mathrm{chord}}, \tag{2}$$

where A_{cell} is the cross-sectional area of the cell relative to the observer, and l_{chord} is the portion of the chord defining the LOS, L_{chord}, passing through the emitting cell. The total remnant emission along L_{chord} is then

$$F_{\mathrm{obs}} = \sum_{L_{\mathrm{chord}}} F_{\mathrm{obs}}^{\mathrm{cell}}. \tag{3}$$

Absorption cross sections are calculated following the formula laid out in Wilms et al. (2000), assuming that intraremnant gas is the primary absorbing medium:

$$\sigma_{\mathrm{cell}} = \sigma_{\mathrm{gas}}^{\mathrm{cell}} = \sum_{\mathrm{Z,i}} A_{\mathrm{Z}}\ a_{\mathrm{Z,i}}\ \sigma_{\mathrm{bf}}(\mathrm{Z,\ i}). \tag{4}$$

Here A_{Z} is the relative abundance of a given element with atomic number Z, $a_{\mathrm{Z,i}}$ is the ionization fraction for a given ion of said element, and $\sigma_{\mathrm{bf}}(\mathrm{Z,\ i})$ is the photoionization cross section of the specified ion. The A_{Z} and $a_{\mathrm{Z,i}}$ are defined within each emitting cell for each epoch of the simulation, while $\sigma_{\mathrm{bf}}(\mathrm{Z,\ i})$ is drawn from `atomdb` when available and Verner et al. (1996) otherwise. The observed emission from each `ChN` cell then becomes

$$F_{\mathrm{obs}}^{\mathrm{cell}} = e^{-\tau_{\mathrm{FG}}} e^{-\sigma_{\mathrm{cell}} N(\mathrm{H})_{\mathrm{cell}}} f(\nu) A_{\mathrm{cell}} l_{\mathrm{chord}}, \tag{5}$$

where τ_{FG} is the summed optical depth of every cell between the emitting cell and the observer,

$$\tau_{\mathrm{FG}} = \sum_{\mathrm{cell}} \sigma_{\mathrm{cell}} N(\mathrm{H})_{\mathrm{cell}}, \tag{6}$$

and

$$N(\mathrm{H})_{\mathrm{cell}} = n_{\mathrm{H}}^{\mathrm{cell}} l_{\mathrm{chord}} \tag{7}$$

is the hydrogen column density, with $n_{\mathrm{H}}^{\mathrm{cell}}$ as the hydrogen number density for the cell.

An interesting consequence of this technique is that we can now map the absorption within the remnant as a function of radius from the center. We can also map the absorption of any particular ion. Unfortunately, the absorption due to lower excited states of many atoms in the unshocked ejecta will likely be underestimated due to the fact that `ChN` does not consider clumping in the ejecta. In the absence of shocks, density increases due to ejecta clumping are one of the main sources of excitation, and neglecting them can lead to significant underestimation of the populations of lower excited states and the expected absorption for excited states outside of the shocked region by extension (Dessart et al. 2018). In spite of this, the total calculated absorption should still produce reasonable results when considering all of the species in the remnant. Absorption within the shocked region, as well as due to more highly ionized elements, should also be less affected by clumping. By examining the absorption along the projected LOSs presented in Figure 1, we can categorize them into two major groups: regions where the LOS passes through the unshocked core and regions where the LOS only passes through the shocked region. The main difference between the two groups is that the optical depth below ∼2 keV is several orders of magnitude higher for those LOSs containing the core region due to the high-density unshocked ejecta from the carbon/oxygen (CO) core of the progenitor.

The dynamical information for each `ChN` cell includes the cell velocity relative to the center of the remnant. From this, we can construct the velocity of the cell relative to the observer. To do this, we take advantage of the spherical symmetry of the remnant models and divide the remnant into two hemispheres along the line where cell velocity is perpendicular to the LOS, as depicted in Figure 2.

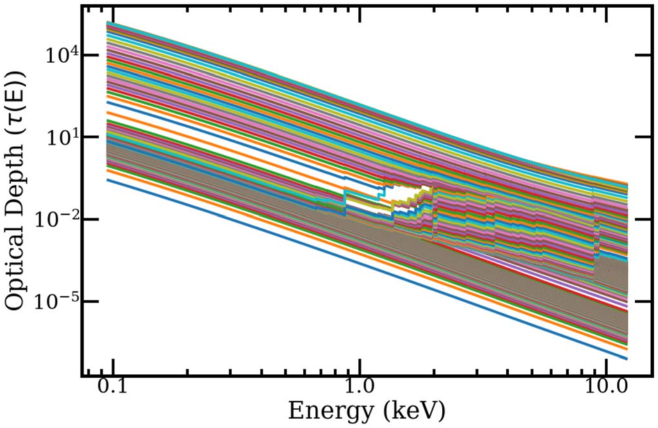

Figure 1. Optical depths along the LOS for a 16 $M_\odot$ model. Each curve corresponds to the optical depth as a function of photon energy for the most distant point in the remnant from the observer along the specified LOS. The low-energy separation in the optical depths is dictated by whether the LOS passes through the unshocked region of the remnant, with the high optical depth LOSs coming from those passing closest to the center of the remnant.

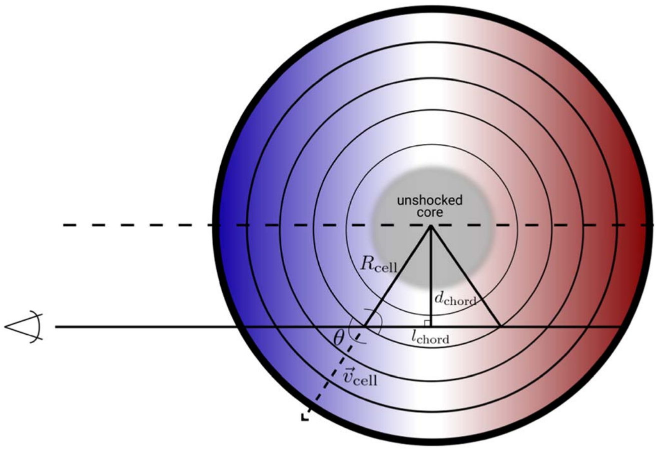

Figure 2. Schematic view of the LOS (solid line) traced out by a ray from the observer through the remnant. We assume that rays from the observer can be treated as parallel through the remnant. The red areas correspond to emitting regions that will appear redshifted to the observer, while the blue regions correspond to blueshifted emitting regions. The symmetry of the model means that the velocity of the emitting regions is purely radial. The optical depths presented in Figure 1 are derived for the point where the defined LOS intersects with the redshifted portion of the FS.

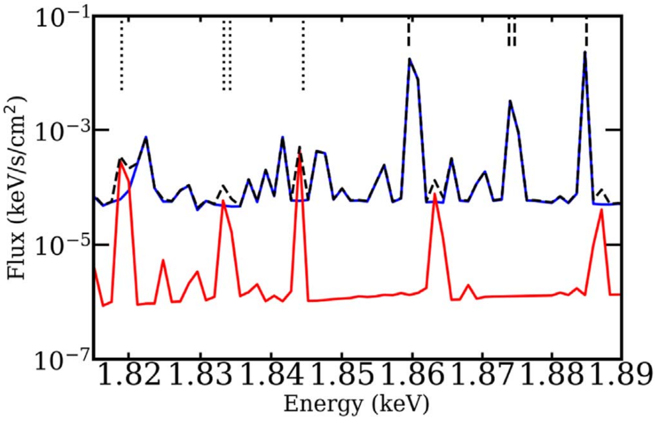

Figure 3. The He-like Si emission from the central LOS for an 11.0 $M_\odot$ zero-age main-sequence (ZAMS) mass star 5 yr post–core collapse. The black dashed curve corresponds to the observed spectrum, while the blue solid curve corresponds to the contributions from the blueshifted component and the red solid curve corresponds to the redshifted component. The redshifted component is strongly absorbed by the unshocked ejecta.

The hemisphere opposite the observer will contain purely redshifted emission, and the hemisphere facing the observer will contain only blueshifted emission. The Doppler shift a given photon energy exhibits is defined as

$$\Delta E = \frac{E_0(1 - \gamma + \beta\cos\theta)}{\gamma(1 - \beta\cos\theta)}, \tag{8}$$

which can be approximated as

$$\Delta E \approx E_0\beta\cos\theta \tag{9}$$

for the vast majority of remnants in the grid. Here $\gamma = (1 - \beta^2)^{-\frac{1}{2}}$, β is the ratio v/c, and θ indicates the angle between the observer LOS and the velocity vector in the source rest frame, with zero indicating motion directly toward the observer, and 180° (π rad) indicating motion directly away from the observer. Each cell can be further divided into regions where the boundaries are defined as the points along l_{chord} where the Doppler shift ΔE can be divided into an integer value of the `ChN` energy bin width ($\Delta E_{\text{bin}} = 1.2$ eV in this paper, but this can be altered) such that

$$\Delta n_{\text{bin}} = \frac{\Delta E}{\Delta E_{\text{bin}}}. \tag{10}$$

2.2. Absorbed Redshifted Emission from the Far Side of the Remnant

The asymmetric nature of the velocity distribution means that redshifted emission will be preferentially absorbed, as the light travel path for that emission is longer than for the blueshifted emission, and the entirety of the additional path is through the remnant. This means that the observed emission is a function not just of the remnant energetics and composition but also of the projected remnant structure. The most obvious examples of redshifted and absorbed emission will occur along LOSs that pass through the core of the remnant. Here the emission will be composed of highly Doppler-shifted components, as their will be few regions with small velocities relative to the LOS, and the redshifted component of the emission will be most absorbed as the redshifted emission passes through the entirety of the unshocked ejecta. An example of this can be seen in Figure 3. The caveat is that these same regions will also be lower-luminosity areas, as a large portion of the emitting volume along the LOS will be the unshocked core and therefore emit little if at all in the X-ray. This can be directly seen by examining the emission measure along the LOS for the remnant shown in Figure 4. The emission measure peaks near the contact discontinuity for our models, which makes sense because that region will contain the bulk of the emitting material, and some of the most recently shocked material will be limb-brightened due to the LOS passing directly through that region. It then drops off as we move inside the reverse shock, and more of the volume along the LOS is composed of the unshocked ejecta. Even in cases where the absorption is relatively low, the relative drop in flux in the redshifted emission can still be detected. The F and I transitions in Figure 5 show how even in the low-absorption region near the contact discontinuity of the remnant, the fact that the emission for this transition is coming mainly from regions near the

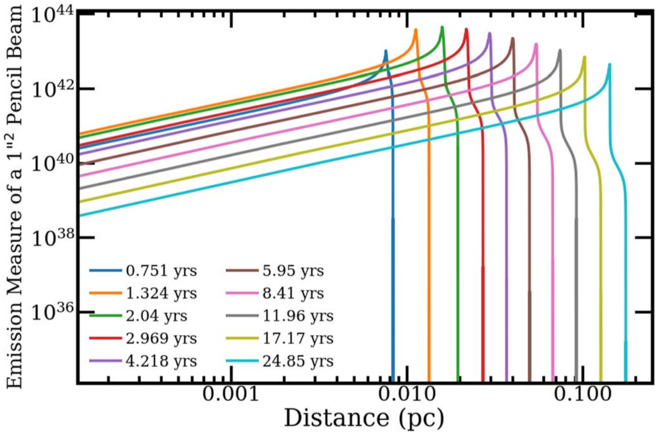

Figure 4. Emission measure along the LOS for a pencil beam passing through various regions of a 15 $M_\odot$ ZAMS mass remnant for several simulation epochs. The emission measure peaks near the contact discontinuity and trails off outside the shocked region.

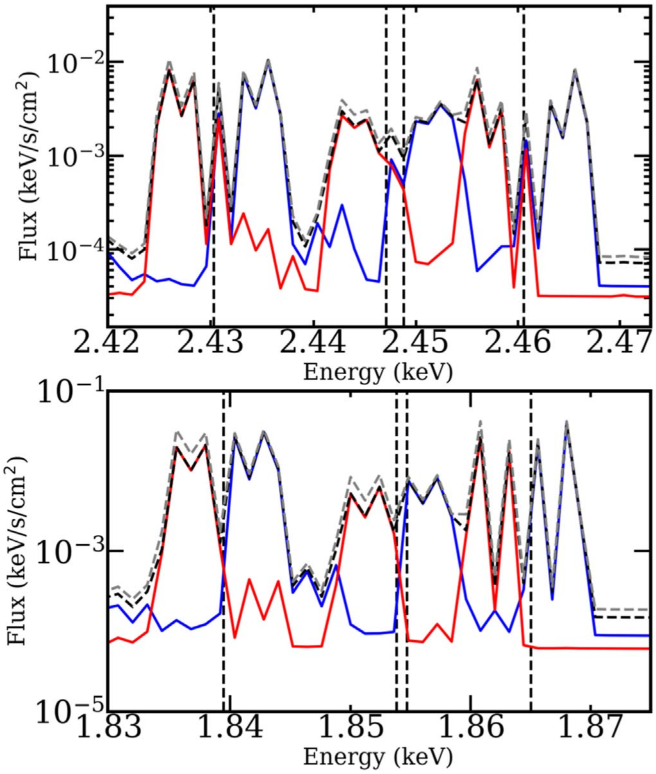

Figure 5. Top: He-like Si features in the LOS spectra of a remnant from a 16 $M_\odot$ star 20 yr post–core collapse. Shown are the LOS spectra with Doppler-shifted (gray dashed), Doppler-shifted and absorbed (black dashed), and red- and blueshifted (red and blue) components of the remnant. Bottom: He-like S features in the LOS spectra of a remnant from a 16 $M_\odot$ star for the same LOS as in the Si case. Both features are in the optically thin regime, but the Si exhibits more absorption than the S. Additionally, the S emission appears to come from a region of the remnant near the center of the LOS, as it exhibits a significant amount of low-velocity emission, while the Si exhibits mainly shifted emission.

forward shock (as evidenced by the clear gaps between the three peaks) causes a discernible drop in flux compared to the expected emission from the redshifted component. Detection of these drops will likely be beyond even next-generation observatories, but asymmetries in real remnants may lead to detectable levels of absorption.

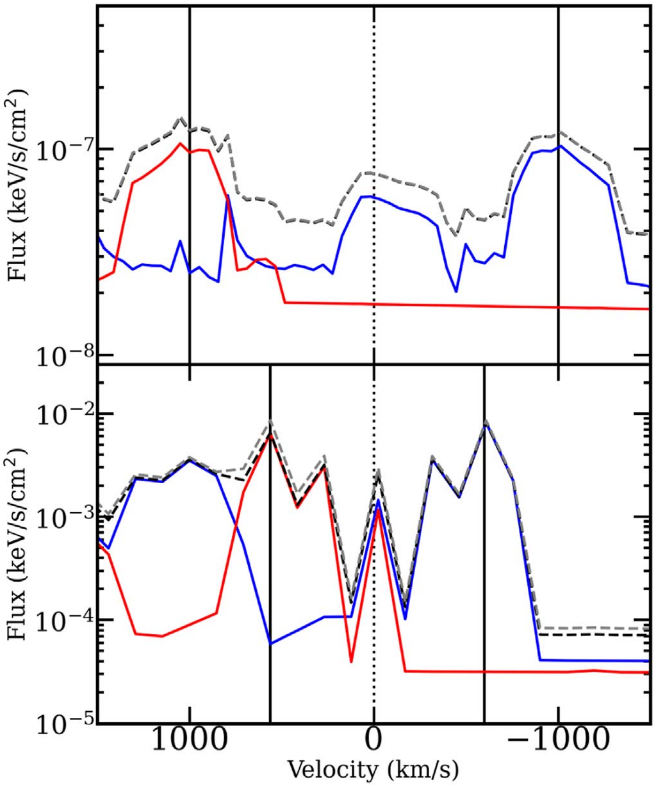

Figure 6. Top: emission from H-like Fe Lyα 1 along a specific LOS plotted in velocity space centered around stationary Lyα 1. Two larger peaks correspond to emission from the line, while the smaller blue peak corresponds to emission from Fe Lyα 2. Bottom: emission from He-like S R along a specific LOS in velocity space centered around stationary R. There is a significant low-velocity component in S (dotted vertical line) with two prominent peaks on either side (solid vertical lines). The low-velocity emission combined with the two prominent peaks indicates that S emission is coming from near the center of the LOS, while the lack of emission in Fe coupled with the fact that the shifted peaks are at a higher velocity indicate that it is coming from the outer edge of the LOS.

Examining the relative Doppler broadening can also give insight into where emission occurs in the remnant. For the LOSs considered in Figures 5 and 6, emission from the three elements considered appears to come from multiple distinct regions. Both Fe and Si appear to have no emission coming from the low-velocity portion near the center of the LOS, as there is no peak near the unshifted emission line in the spectrum, while S has a prominent peak. This is further supported by the fact that the Fe has a much higher velocity than the S, indicating that it is coming from a region closer to the forward shock and nearer to the edge of the remnant.

3. Application to Next-generation X-Ray Missions

The next generation of X-ray telescopes equipped with microcalorimeters is expected to offer unprecedented spectral resolution across the 0.1–10 keV range. These missions will also offer fairly large fields of view (FOVs), allowing for many objects to be imaged simultaneously. Unfortunately, these missions will not have the spatial resolution that has become one of the hallmarks of the Chandra mission. Because of this, it is important to understand how the spatially unresolved spectra can be used to extract information about the physical configuration of the remnant. The two next-generation instruments scheduled to fly, XRISM and Athena, will not be able to

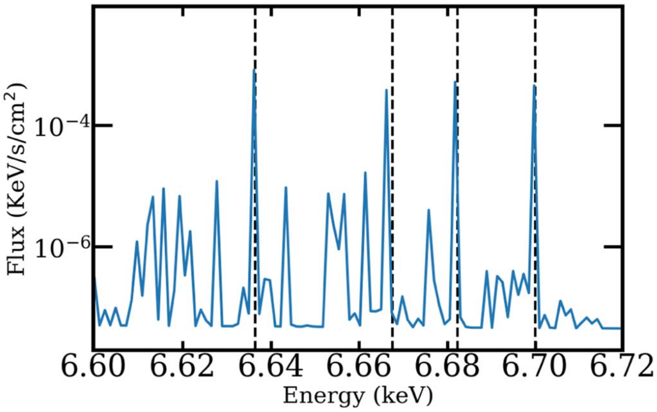

Figure 7. The Fe K emission from an unmodified 20 $M_\odot$ `ChN` model ∼2000 yr post–core collapse. The four He-like transitions are noted with vertical lines. The rest-frame separation of these lines is sufficiently large for a microcalorimeter to resolve.

spatially resolve any of our model remnants beyond ∼10 kpc. This means that any observations of extragalactic remnant populations with these instruments will be strictly point sources.

3.1. The Complexity of the Integrated X-Ray Spectra

Doppler-broadened emission features have long been used by optical astronomers to measure shock velocity and absorption within the remnant. Similarly, X-ray features can be used, with the caveat that oftentimes, these individual transitions are not as isolated as in the optical case. Examining the behavior of simulated remnant spectra when considering the integrated spectra from the 2D projection on the sky allows us to better understand what information can be gleaned from high spectral but low spatial resolution instruments, as well as what the resulting challenges will be. We will begin with a discussion of the He-like Fe transitions in the Fe K complex. The Fe K centroid is a useful discriminant of SNR progenitor type, and its relative isolation from other elemental emission lines makes it easy to measure with current X-ray missions (Yamaguchi et al. 2014). The He-like transitions presented in Figure 7 consist of four bright lines (resonance, forbidden, and the intercombination doublet) spanning 6.65–6.700 keV. When viewed from a stationary source relative to the observer, the most isolated pair of the four distinct lines (R and F) have a separation of 63.5 eV. That is more than sufficient for a microcalorimeter to resolve the two lines. Problems do arise, however, when considering emission from an SNR shock. For a shock moving at ∼3000 km s^{-1} with a velocity vector angled at ∼30° to the observer's LOS, the expected Doppler shift of a line at 6.6 keV is 33 eV. That means that the redshifted component of the R transition and the blueshifted component of the F transition are likely to overlap near the I doublet. This can result in a much more complicated spectrum, especially when considering the fact that for a spherically symmetric remnant, there is emission coming, to varying degrees, from all possible LOS velocities between zero and the true shock velocity. We have plotted a visual representation of this complexity in Figure 8, which contains the Fe K emission for all of the summed LOSs for a 20 $M_\odot$ model for one epoch. It is not immediately obvious what the final summed structure will look like based on the individual spectra, aside from the width of the expected complex in energy space, but it is clear that discerning the individual Fe lines will not be as simple as in the stationary emitter case. In fact, what can often happen is that the expected horned structure for the Doppler-broadened lines can overlap other transitions such that the peak of the horn appears to be emission from the other transition. Extracting spectral information from these complexes will be an important part of interpreting the XRISM and Athena observations. As such, we take care to discuss subtleties in the model spectrum that can be used to discern remnant structure and dynamics, as well as note potential confusion that can be caused by line blending.

For lower Z ions, like the He-like Si depicted in Figure 9, the blending can be quite extreme, and identifying all of the emission lines can be difficult, as the narrower line separations can lead to issues like intermediate energy lines such as the I doublet being completely blended out by emission from surrounding features. We will spend more time discussing what can be discerned from these elements, as they will be important for microcalorimeter missions, but we begin by discussing the Doppler-broadened Fe spectra presented in Figure 10, as the line separation allows us to uniquely identify at least some components from all of the He-like transitions. The broadened Fe features in both modeled spectra exhibit the clear double-horned structure expected of a spherically symmetric remnant (Lee et al. 2014; Alp et al. 2018). This is most easily seen in the F transition, which is more isolated from the other three lines, although its blueshifted peak also has some contributions from the redshifted component of one of the I lines. The isolation of the F transition is something that occurs in the He-like states of other elements like Si and S. The interplay between the R and the I doublet, as well as between the two lines in the I doublet, is more complex. In the case of our 20 $M_\odot$, the smaller shock velocity meant that the peaks did not quite overlap the adjacent transitions, but it did put several components in close proximity. The blueshifted component of the I1 transition is close enough to the stationary R transition that it could be mistaken for a slightly redshifted component from the R transition. Additionally, the redshifted R component and the blueshifted I2 component frame the I1 transition in such a way that it could be easily interpreted as the horned structure of the I1 transition. When the shock velocity is higher, we can arrive at other interesting configurations. In the case of the 16 $M_\odot$ model, the I transitions and the R transition overlap to make it appear as though there are unshifted peaks for all three of the transitions. What actually happens is that the blueshifted component of the I2 transition and the redshifted component of the R transition exactly overlap at the I1 transition rest energy. The redshifted component of the I1 transition likewise overlaps the I2 transitions (with some small contributions from the F transition, discussed below). Finally, the blueshifted component of the I1 transition overlaps the R rest energy.

There are two additional spectral features worth mentioning for He-like Fe. For the spherically symmetric remnant, Fe is ionized to Fe XXV in the area near to the two shock fronts. This results in two Fe XXV–emitting shells with distinct velocity profiles. The one near the RS is slower than the FS but with a higher density. This results in two distinct horned structures in the spectra related to the two emitting regions. These are easiest to see in the F transition, which has two visible redshifted peaks, and the R transition, which has two visible blueshifted peaks. The peaks for the R transition are more obvious because there are no major satellite lines that have the necessary flux to produce the peak in the plots just below −2000 km s^{-1}. From

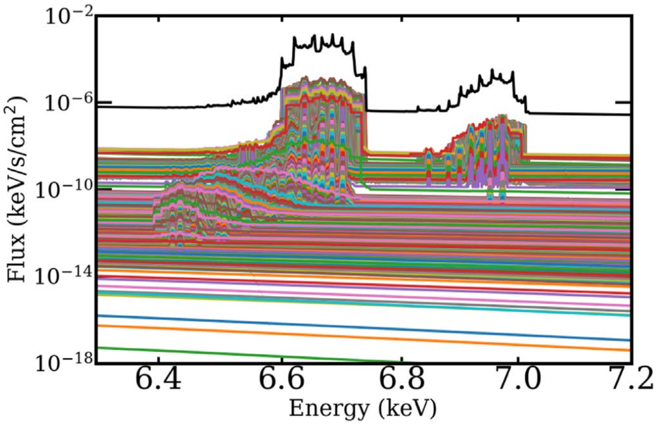

Figure 8. Individual LOSs that contribute to the total integrated spectrum (black curve) for He-like (6.6–6.7 keV) and H-like (6.8–7 keV) Fe. It quickly becomes clear that Doppler broadening can complicate the expected spectrum.

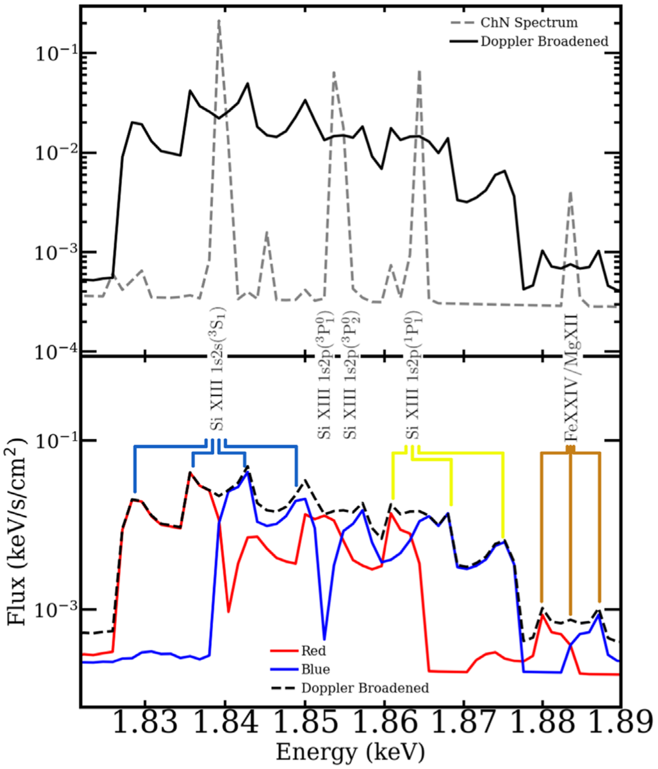

Figure 9. The He-like Si features for the 16 $M_\odot$ remnant at ∼2000 yr post–core collapse. The smaller ΔE between the I transitions results in them appearing as a single line. The complex is also much closer in energy space, resulting in a significant amount of blending between the three lines and making it difficult to identify any features definitively belonging to I. A single line corresponding to two transitions with similar emissivities (Mg XII/Fe XXIV) can be seen at the far right. The forbidden line is still easily identified, along with the blueshifted components of the resonance line.

this, we can infer that this is coming from a faster component of the remnant than the peak we discussed in the preceding paragraph. This, combined with the lower flux for the shifted line, implies that this corresponds to the Fe XXV population near the FS, and the other peak corresponds to the population near the RS. The same inference can be made when examining the F transition, although the higher-energy satellite lines near the F transition do contribute slightly. The FS F transition also contributes to the emission at the I2 transition, along with some of the brighter satellite lines.

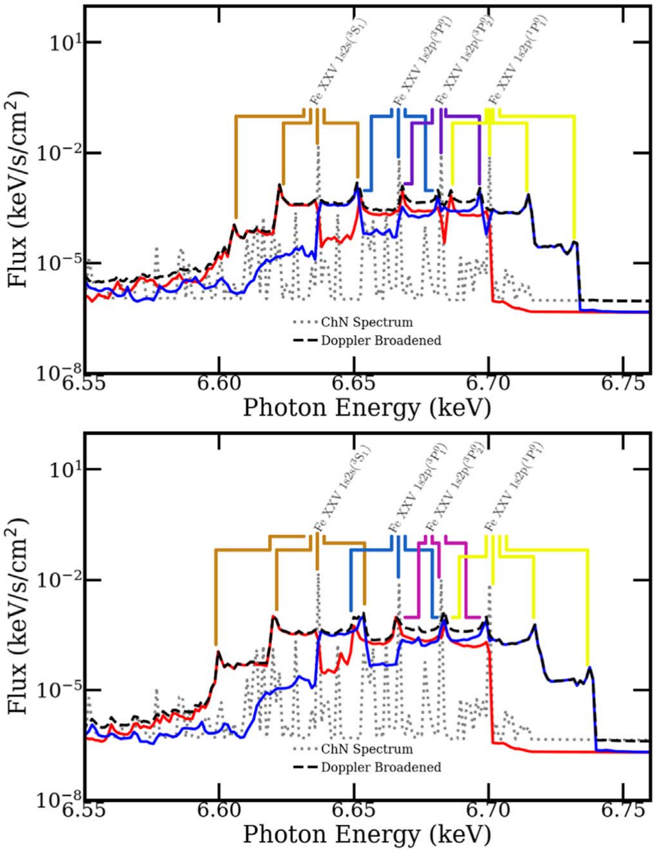

Figure 10. Top: spectrally resolved Fe K complex of a spatially unresolved 2000 yr old remnant evolved from a 20 $M_\odot$ ZAMS mass star. Bottom: Fe K complex of a 2000 yr old remnant from a 16 $M_\odot$ ZAMS mass star. Including Doppler broadening makes identifying spectral features more difficult. For the lower-mass progenitor, the intercombination doublet and the resonance transition have components that overlap exactly at the unshifted values for other lines, giving the appearance of more low-velocity regions than actually exist. The higher-mass progenitor results in small horn structures around unshifted line energies that are unrelated to the unshifted line, as can be seen for the Fe XXV 1s2p (^{3}P$^0_2$) transition. The two peaks are actually the shifted components of the two neighboring Fe XXV lines.

The He-like Si is similarly complex, especially around the intercombination line, as can be seen in Figure 9. Similar behavior can still be discerned, especially in the F and R transitions. What is particularly interesting about the spectrum near He-like Si is a single line at 1.885 keV. This line is not associated with Si and is actually two transitions from Mg XII and Fe XXIV with the same energy. This combined line shows little contamination from other transitions and clearly exhibits the horned structure resulting from the RS motion.

Unlike in the Fe case, the rest-frame intercombination lines in both Si XIII and S XV are not sufficiently separated from each other to be resolved as separate lines at an energy resolution of 3 eV. They are also significantly closer to the R transition than in Fe XXV, which results in significant muddling of the spectrum between the F and R transitions. Looking at Figures 9 and 11, it is not immediately obvious where the intercombination lines exist in the He-like complexes of S and Si. Additionally, the R transition can also be more difficult to locate as it is closer to the doublet than the F transition. Forbidden-line emission is still relatively easy to identify in all cases, making it the most useful for determining velocity

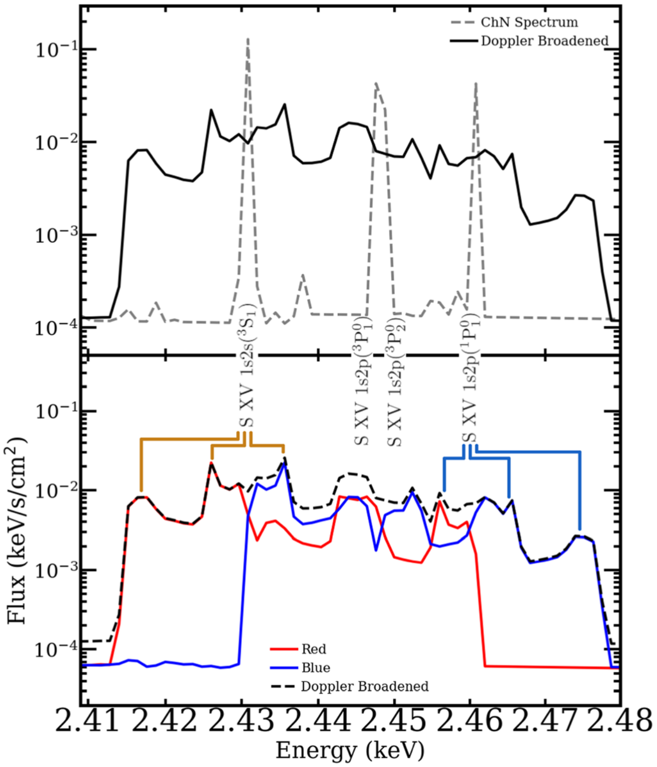

Figure 11. The He-like S features for the 16 $M_\odot$ remnant at ∼2000 yr post–core collapse. Much like in the Si case, the smaller ΔE between the I transitions results in them appearing as a single line, and the blending makes it difficult to identify any features definitively belonging to I. The forbidden line is still easily identified, along with the blueshifted components of the resonance line.

information. We put this to the test by examining the derived velocities of the FS and RS from the F transitions in Fe, S, and Si. We see marginal differences in the derived velocities, likely due to subtle differences in where the velocity distribution peaks relative to the shocks. We also note that the horned structure is more sharply defined for higher-Z elements, as depicted in Figure 12.

All of the previous commentary comes with the caveat that we do not include thermal broadening in any of the spectra. To confirm that thermal broadening would only have a mild effect on the final spectra, we calculated the expected FWHM for a line at 6.6 keV assuming an ion temperature of 10^7 K and that the ion mass corresponds to hydrogen (the broadening will scale roughly as $A^{-\frac{1}{2}}$ for larger ions and $T^{\frac{1}{2}}$ for higher temperatures). This results in an FWHM of ∼15 eV, which means that the thermal shift for either emitting component will be a factor of ∼4 smaller than the Doppler shift for our models. Given that the lines in Si and S are only spaced by ∼10–20 eV, the broadening would be noticeable in isolation, but the Doppler broadening described above will be the primary driver of broadening. This expected thermal broadening is also on the order of ∼twice the spectral resolution of most next-generation X-ray missions, further limiting its effect on the observed spectrum.

3.2. Simulated Spectral Observations

3.2.1. Extragalactic Sources

The emission of highly ionized high-Z elements is often considered as a useful diagnostic for the plasma conditions of high-energy systems. It has already been proven that Hitomi had the required spectral resolution to discern emission from the He-like Fe transitions in the Fe K complex (Hitomi Collaboration et al. 2016). We also found in Paper I that XRISM should be able to resolve the same transitions in remnant spectra when considering no additional thermal or Doppler broadening. The added complexity of the broadening requires that we revisit these simulations and examine the spectra to better understand what would be expected of an unresolved remnant as viewed on the sky.

In order to properly characterize the ability of future missions to observe these modeled remnants, we employ the `simX` software package. It allows for simulated observations, including instrument response, and other observational effects, including individual photon simulation, for both extended and point sources at any point in the instrument FOV. For simplicity, we assume that the remnant is at the center of the focal plane and simulate multiple observations assuming sources at $d \sim 60$ kpc. We focus on emission from He-like S and Si, as these emission lines occur near the peak effective area for both of the instruments considered, and emission around ∼6.5 keV is not well detected at the SMC for the example remnants when considering broadening, as can be seen in the XRISM spectrum presented in Figure 13. This is consistent with the results in Paper I, which showed that unshifted lines were detectable at the SMC and might mean that emission from lower-velocity Fe regions should still be detectable. We also examine the 3D ionization structure of the remnant using the unabsorbed He-like ratios for each emitting cell and compare the expected distribution to what is derived using the relative broadening and absorption of the He-like line fluxes for the integrated remnant spectrum.

We begin by examining the broadened and baseline spectra generated using simulated 300 ks observations near the peak effectiveness of the Athena detector for the two 16 $M_\odot$ models. Figure 14 allows us to compare the broader spectral features of the broadened and rest-frame spectra and note that the Si and S complexes are still well defined, with comparable luminosities. We examine the complexes in detail in Figure 15, where we can see the blended emission line structure, as was noted in Section 3.1. The lower spectral resolution of the simulated detector further adds to the blending, but the forbidden-line emission is still detectable. The blending is also a useful metric, as this level of blending requires the intercombination line to be of the same order of magnitude as the forbidden and resonance lines indicating the ionization state of the remnant (Porquet et al. 2010).

We similarly examined the same remnant as viewed by the XRISM mission. Because of XRISM's lower collecting area, we extended the observation to 1 Ms but otherwise kept the parameters the same. We present the results for Si and S in Figure 15. The slightly lower spectral resolution led to a modest increase in blending, but the forbidden-line emission was still detectable. Identifying the blueshifted component of the R transition is more difficult than in the Athena case, but there is still discernible structure beyond the more Gaussian-like complexes observed by Chandra and other CCD missions.

Velocities can be extracted by fitting a Gaussian to the high-velocity components for the F and R transitions and using their shift from the line's rest energy to calculate the average velocity for the remnant. For many remnants, we can take the extracted velocities and reliably assign these values to the

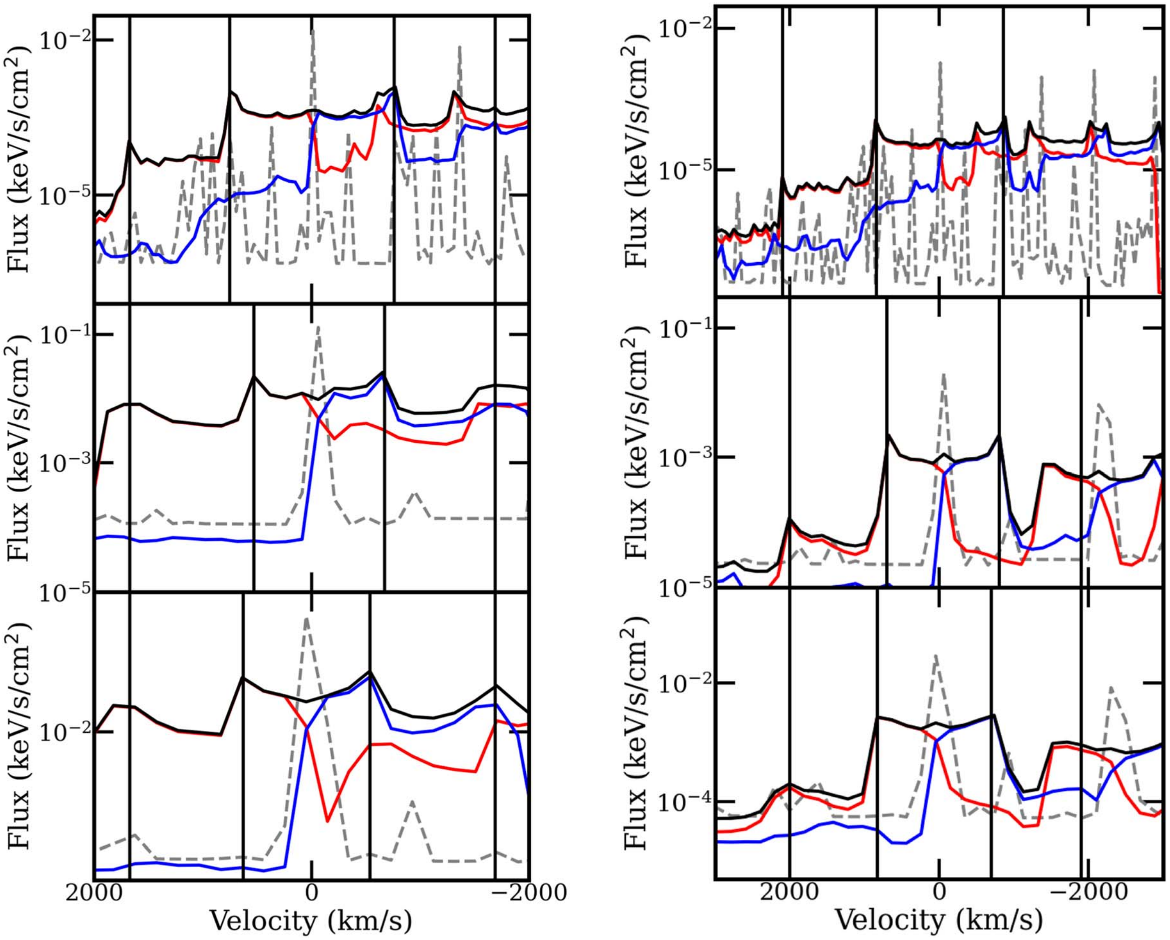

Figure 12. Comparison of forbidden-line emission for Si, S, and Fe (bottom to top) features for the 16 $M_\odot$ slow wind case (left) and fast wind case (right). There are two distinct horn structures corresponding to emission from the RS (lower-velocity horn) and FS (higher-velocity horn). Only the redshifted component of the FS emission is easily identified, as the blueshifted component interacts with emission from the intercombination lines along with other satellite lines in some cases. The relative velocities may indicate approximately where the emission is coming from relative to the shock, with lower velocities indicating emission occurring closer to the RS.

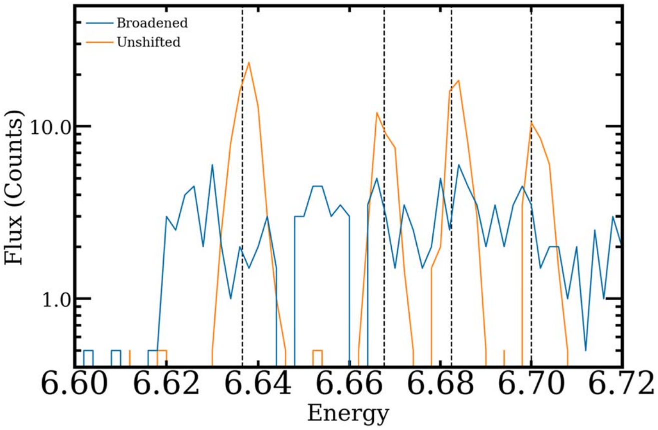

Figure 13. The XRISM 1 Ms exposure of the integrated spectrum for a 16 $M_\odot$ remnant centered on Fe K. The He-like Fe is clearly visible in the unbroadened spectrum, but the blending of lines in the broadened case lowers the overall flux to the point where the Fe is barely detectable. A similar result occurs in the Athena spectrum.

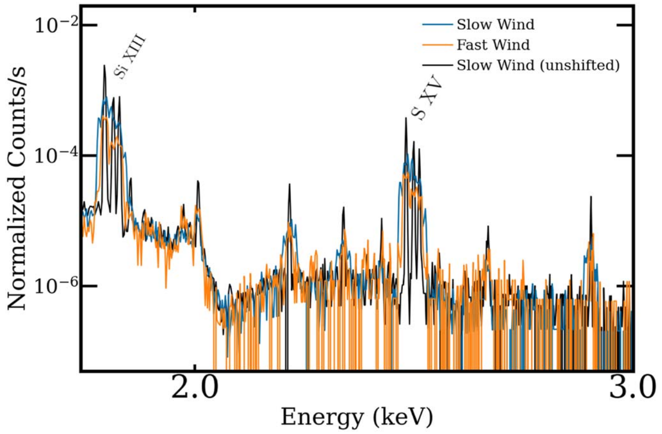

Figure 14. Athena 300 ks exposure of the integrated spectra for a 16 $M_\odot$ remnant in both a fast ($v = 15$ km s^{-1}) and a slow ($v = 5$ km s^{-1}) wind. The S and Si K complexes are resolved in both cases. The slow wind case results in overall brighter spectra, but we have normalized all spectra such that their integrated flux is 1.

plasma velocities at the respective shocks. This is due to the fact that at sufficiently late times, the remnant can be approximated by a thin shell, with the highest-velocity components of the emission coming from LOSs along the center of the remnant. For younger remnants, limb brightening is still an important consideration; thus, we cannot extract the exact velocity from the highest-velocity components due to the emission being dominated by LOSs centered in the shock itself.

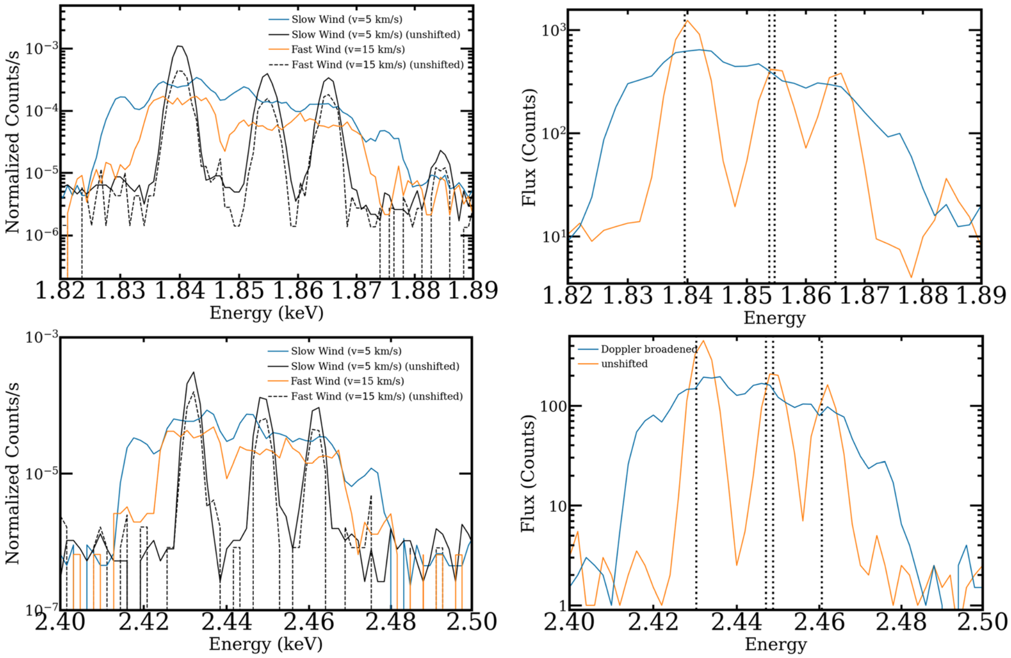

Figure 15. Left: simulated Athena observations for Si XIII K (top) and S XV (bottom) for a 16 $M_\odot$ ZAMS remnant in the SMC ($d = 60$ kpc). The lower density of the fast wind results in far less emission from the higher-velocity horn corresponding to the FS. The RS horn still shows a similar velocity profile, likely resulting from the identical ejecta composition for the two remnant models. The I and R transitions are almost entirely washed out in both broadened spectra, with the doublet appearing as a single line even in the unshifted case. The Mg XII/Fe XXIV line is also lost in the noise. Right: simulated XRISM observations for Si XIII K (top) and S XV (bottom) for a 16 $M_\odot$ ZAMS remnant in the SMC ($d = 60$ kpc). The F transition is still detectable, like in the Athena spectra, while the I and R transitions are similarly washed out in the broadened spectra.

For these remnants, velocities can be extracted based on estimating where the dominant LOSs are located within the remnant. We discuss how this particular piece can be parsed in greater detail by examining emission from the outer edges of the remnants in Section 3.2.2.

As an example, we extract velocities from the slow wind 16 $M_\odot$ model discussed in Figure 15. The fits for the lines are displayed in Figure 16, and the extracted velocities are tabulated in Table 1. The 16.0 $M_\odot$ at 1000 yr is in the regime where we can approximate emission as coming from a thin shell and thus assume that the two velocities measured for each line correspond to the FS (higher-velocity measurement) and RS (lower-velocity measurement). The assumption does not completely hold due to the fact that the emitting regions are not right on the edge of the shocks, and the measured velocities differ slightly due to the emission from each transition being dominated by a different region. Additionally, blending with the intercombination line, we are only able to extract the redshifted component from the F transition and the blueshifted components from the R transition. Even with this limitation, we are still able to reliably extract line components and make reasonable measurements of plasma velocities.

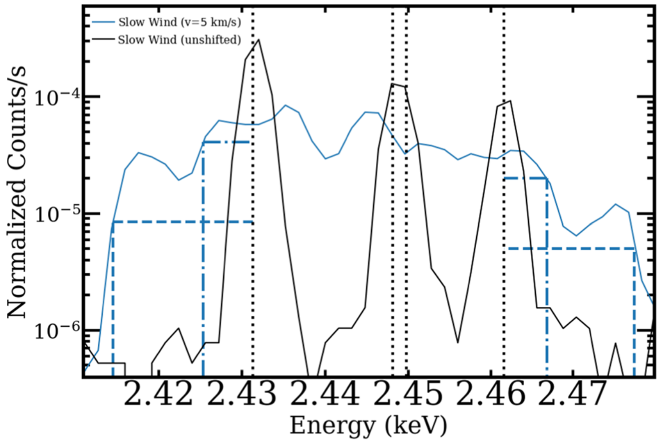

Figure 16. Athena simulated spectra of the 16 $M_\odot$ SMC remnant with the shifted F and R transitions marked against the respective rest-frame lines. In both cases, we have marked the shift due to the FS and RS. Due to overlap with the other lines, we are only able to extract the redshifted component of the F transition and the blueshifted component of the R transition.

3.2.2. Galactic Sources

When considering Galactic sources, proposed missions such as a rescoped Athena or the proposed Line Emission Mapper will be capable of resolving the shock structure of remnants with large angular sizes while simultaneously measuring the line structures. This allows us to examine a smaller range of LOS velocities, greatly reducing the complexity of broadened emission from the He-like state, and the relative proximities (∼5 kpc) of Galactic remnants allow for roughly a factor of 10 reduction in exposure times compared to extragalactic sources. We can see this clearly in Figure 17. Here the broadening is evident when compared to the original `ChN` spectra, but the individual emission lines from He-like Si are still distinguishable, even at a relatively modest exposure of 10 ks. The ionization of these remnants does not indicate a strongly recombining plasma, meaning that the relative intensities of the three He-like transitions are not comparable, and there is less blending due to the intercombination line infringing on the other transitions. Given an estimate of the distance to the remnant, an observation of the outer rim beginning from the edge of the FS can be used to derive plasma velocities for the innermost LOS in the observed region under the assumption

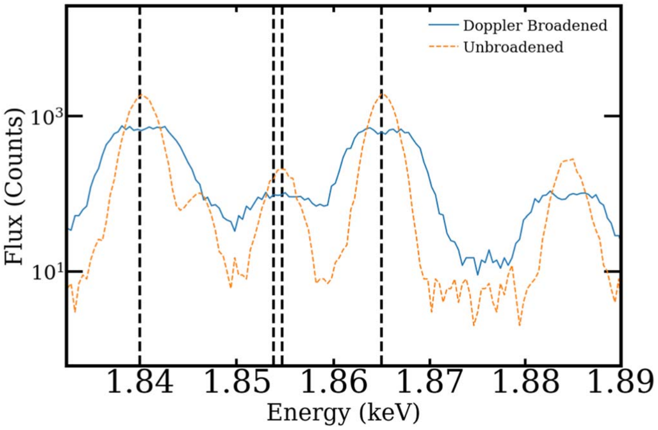

Figure 17. Athena simulation of the He-like Si complex extracted from the outer 20″ of the 16.0 $M_\odot$ remnant 150 yr post–core collapse. At these early times, the entire shock is contained within the 20″, but the high-velocity components from interior LOSs are absent.

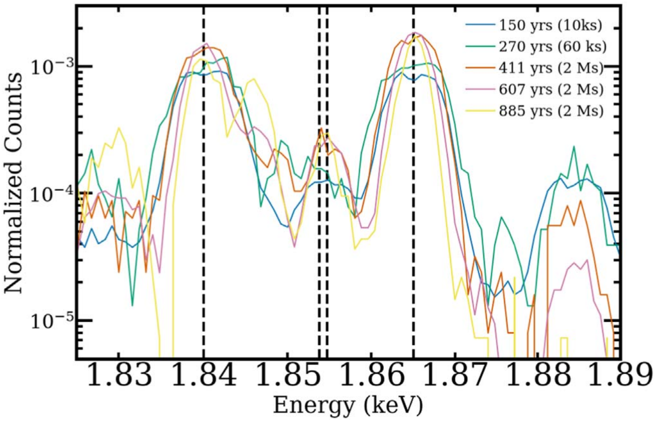

Figure 18. Athena simulation of the He-like Si complex extracted from the outer 20″ of the 16.0 $M_\odot$ remnant for several epochs post–core collapse. At these early times, the entire shock is contained within the 20″, but the high-velocity components from interior LOSs are absent. As the remnant ages and expands, a smaller fraction of the shock exists in the outer 20″ of the remnant, and the velocity relative to the LOS for the portion within the region also decreases, resulting in less broadening even though the average plasma velocity has not changed significantly.

Table 1
He-like S Velocities for the Integrated Spectra of a 16.0 $M_\odot$ SN

Line	ΔE (eV)	$v \cos\theta$[a] (km s^{-1})	$v_{\rm expected}$[b] (km s^{-1})
F (RS)	6.0 ± 0.3	740 ± 37	725
F (FS)	16.7 ± 0.3	2060 ± 37	1946
R (RS)	5.2 ± 0.5	633 ± 60	725
R (FS)	15.9 ± 0.5	1938 ± 60	1946

Notes.

[a] For remnants with sufficiently small emitting regions, we can assume $v \cos\theta = v$.

[b] Here $v_{\rm expected}$ assumes that the emitting region is at the edge of the shock; in reality, emission for the transitions peaks slightly interior.

that the remnant is reasonably close to spherically symmetric within the observing region. As a proof of concept, we explore simulated Athena spectra for the outer 20″ of a 16.0 $M_\odot$ remnant 5 kpc from Earth at several epochs beginning 150 yr post–core collapse. For these remnants, we focus on He-like Si, as it is one of the highest-Z elements whose He-like states are below the 2 keV dropoff in effective area for Athena. The full He-like complex is shown in Figure 18 for each epoch, with the accompanying exposure time. One important thing to note is that as the remnant ages, the fixed observing region being examined covers a smaller fraction of the total shocked region for the remnant. At 150 yr, the full shocked region is observed, while at 885 yr, only a small fraction of the FS is contained in the 20″ region.

By measuring the line widths, we can estimate the velocity along the LOS using Equation (9). We can then calculate the physical distance spanned by the observing region and make an estimate of the plasma velocity by using the fact that expansion is radially outward from the center of the remnant and assuming that the emission is dominated by the innermost LOS. In Figure 19, we show several examples of line measurements we have extracted from the Si F and R transitions, and we record the results in Table 2.

In general, the F transition seems to provide lower velocities than the R transition. Physically, this could be due to small variations in where emission is being generated, with the emission from the forbidden line coming from regions shocked earlier in the remnant's life, which have now begun recombining and decelerating slightly when compared to the regions dominated by the R transition. For the 270 and 411 yr epochs, the velocities derived from the R and F transitions match well with what is expected from the velocity at the innermost LOS. The 607 yr remnant underestimates the velocity slightly, likely due to how small the velocity is relative to the innermost LOS.

The earliest epoch is harder to estimate due to it spanning beyond the shocked region, as well as the lower ionization in the first epoch of the `ChN` simulation. At these early times, we would expect He-like Si emission to come only from areas close to the two shocked regions, meaning that our method for calculating the true velocity will overestimate the fraction of the velocity along the LOS and lead us to underestimate the true velocity. At 885 yr, the broadening due to remnant expansion is smaller than the spectral resolution of Athena. Examining the outer rims of galactic SNRs in a similar fashion could complement existing expansion rate studies like those performed on G266.2–1.2 (e.g., Allen et al. 2015) by providing an independent velocity measurement for a given region. They would also allow expansion rates to be estimated based on a single observation, as opposed to measuring the change over multiple epochs.

The archetypal young Galactic CCSN remnant is Cassiopeia A. While the distribution of ejecta in Cas A is quite asymmetric in X-rays (e.g., Hughes et al. 2000; Sato et al. 2021), with evidence for overturning of ejecta in certain regions as the shock propagated through the progenitor, our grid of 1D models may still prove to be valuable when considering the evolution of ejecta along certain radial directions (the so-called "radial flow" approximation). It is likely that no single model presented here can reproduce the bulk properties of an asymmetric object such as Cas A, though a suitable combination of models, constrained by the observable properties of the ejecta energetics and composition, might be possible. Certainly, with future X-ray microcalorimeter missions with moderate spatial resolution, measuring the Doppler broadening along different radial directions will provide measurements that are directly comparable to these models.

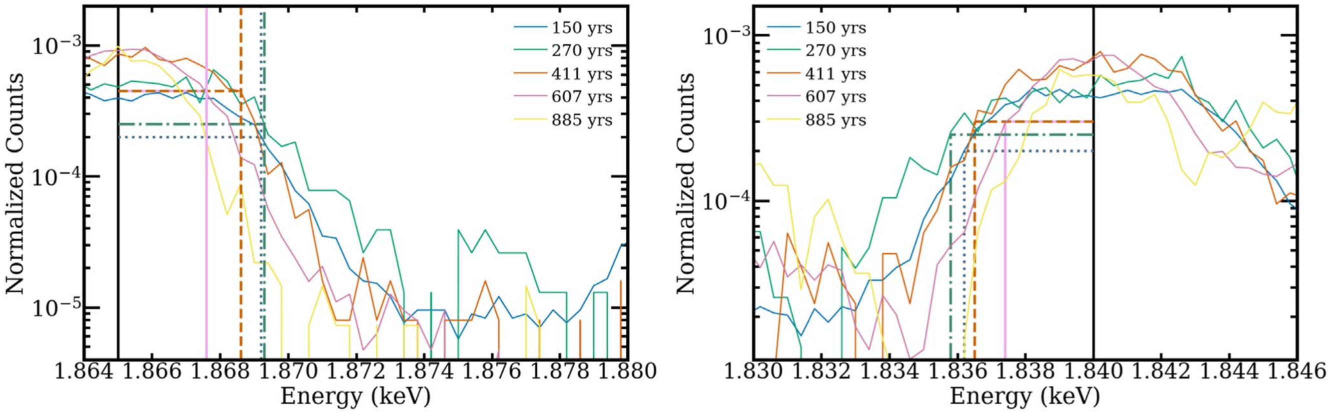

Figure 19. Top: spectrally resolved resonance (R) line for He-like Si for the outer 20″ of a 16 $M_\odot$ ZAMS mass star for several observing epochs post–core collapse. Bottom: spectrally resolved forbidden (F) line for He-like Si for the outer 20″ of a 16 $M_\odot$ ZAMS mass star for several observing epochs post–core collapse. The vertical and horizontal lines correspond to the FWHM of the line for each epoch. When considering smaller fractions of the remnant, where the component of the velocity parallel to the LOS is small, it is possible to resolve individual emission lines while still extracting useful information about plasma velocity.

Table 2
He-like Si Velocities for the Outer 20″ of a 16.0 $M_\odot$ SNR

Age (yr)	ΔE (F) (eV)	ΔE (R) (eV)	$v\cos\theta$ (F) (km $\mathrm{s^{-1}}$)	$v\cos\theta$ (R) (km $\mathrm{s^{-1}}$)	v (F) (km $\mathrm{s^{-1}}$)	v (R) (km $\mathrm{s^{-1}}$)	v_{expected}
150	3.8 ± 0.1	4.2 ± 0.1	619 ± 16	675 ± 16	1528 ± 40	1666 ± 40	…[a]
270	4.2 ± 0.1	4.3 ± 0.1	684 ± 16	692 ± 16	2478 ± 59	2503 ± 58	2525
411	3.5 ± 0.1	3.6 ± 0.1	571 ± 16	595 ± 16	2178 ± 62	2211 ± 61	2208
607	2.6 ± 0.2	2.6 ± 0.2	358 ± 32	418 ± 32	1823 ± 140	1798 ± 139	2054
885[b]	…	…	…	…	…	…	…

Notes.
[a] At 150 yr, the emitting regions are narrow, and the inner LOS is not representative of the dominant emitting region.
[b] At 885 yr, the broadening due to the velocity relative to the LOS is smaller than the spectral resolution of Athena.

4. Summary and Future Work

Intraremnant absorption can play an important role in shaping the SNR spectrum. Examining the broadened emission and looking at the relative differences between the redshifted and blueshifted components of spectral features can yield information about the composition and density of the remnant. High-resolution spectra from next-generation observatories can also be used to probe the ionization state of the remnant by comparing the relative Doppler broadening and absorption of X-ray emission lines. This is especially important for determining 3D structure when the remnant cannot be spatially resolved. Blending due to high-velocity broadening will complicate spectral interpretations, but it is still possible to extract information from these spectra. In regimes where He-like emission lines for a given element are not comparable in strength, blending will be less of an issue, and more detailed information can be extracted. Future work will need to be done to understand what the spectra from remnants with more complex circumstellar environments will look like, as large changes in density and shock velocity will lead to different spectra than the wind-like CSM cases considered here.

Acknowledgments

T.E.J. acknowledges support from NASA Astrophysical Theory Program No. 80NSSC18K0566. He additionally acknowledges support from the Chandra X-ray Center, which is operated by the Smithsonian Institution under NASA contract NAS8-03060. S.H.L. is supported by JSPS KAKENHI grant No. JP19K03913 and the World Premier International Research Center Initiative (WPI), MEXT, Japan. D.M. acknowledges National Science Foundation support from grants PHY-1914448 and AST-2037297. This work was partially supported by JSPS Grants-in-Aid for Scientific Research "KAKENHI" (A: grant No. JP19H00693). S.N. wishes to acknowledge support from the RIKEN Program of Interdisciplinary Theoretical and Mathematical Sciences (iTHEMS) and the RIKEN Pioneering Program for Evolution of Matter in the Universe (r-EMU). Some of the computations in this paper were conducted on the Smithsonian High Performance Cluster (SI/HPC), Smithsonian Institution (https://doi.org/10.25572/SIHPC). This work made use of the following software packages: MatPlotLib (Hunter 2007), NASA ADS, NumPy (van der Walt et al. 2011), Pandas (McKinney 2010).

Data Availability

The data sets generated for this paper will be available in the gitlab group pre-ccsne-wind at https://gitlab.com/pre-ccsne-wind.

ORCID iDs

Taylor Jacovich https://orcid.org/0000-0003-0226-0343
Daniel Patnaude https://orcid.org/0000-0002-7507-8115
Patrick Slane https://orcid.org/0000-0002-6986-6756
Carles Badenes https://orcid.org/0000-0003-3494-343X
Shiu-Hang Lee https://orcid.org/0000-0002-2899-4241

Shigehiro Nagataki https://orcid.org/0000-0002-7025-284X
Dan Milisavljevic https://orcid.org/0000-0002-0763-3885

References

Allen, G. E., Chow, K., DeLaney, T., et al. 2015, ApJ, 798, 82
Alp, D., Larsson, J., Fransson, C., et al. 2018, ApJ, 864, 175
Barret, D., Lam Trong, T., den Herder, J.-W., et al. 2016, Proc. SPIE, 9905, 99052F
DeLaney, T., Rudnick, L., Stage, M. D., et al. 2010, ApJ, 725, 2038
Dessart, L., Hillier, D. J., & Wilk, K. D. 2018, A&A, 619, A30
Flanagan, K. A., Canizares, C. R., Dewey, D., et al. 2004, ApJ, 605, 230
Foster, A. R., Smith, R. K., & Brickhouse, N. S. 2017, in AIP Conf. Ser. 1811, Atomic Processes in Plasmas (APiP 2016) (Melville, NY: AIP), 190005
Fransson, C., Larsson, J., Spyromilio, J., et al. 2013, ApJ, 768, 88
Hughes, J. P., Rakowski, C. E., Burrows, D. N., & Slane, P. O. 2000, ApJL, 528, L109
Hunter, J. D. 2007, CSE, 9, 90
Hitomi Collaboration, Aharonian, F., Akamatsu, H., et al. 2016, Natur, 535, 117
Jacovich, T., Patnaude, D., Slane, P., et al. 2021, ApJ, 914, 41
Lee, S.-H., Patnaude, D. J., Ellison, D. C., Nagataki, S., & Slane, P. O. 2014, ApJ, 791, 97
McKinney, W. 2010, in Proc. of the 9th Python in Science Conf., ed. S. van der Walt & J. Millman, 51
Milisavljevic, D., & Fesen, R. A. 2008, ApJ, 677, 306
Milisavljevic, D., & Fesen, R. A. 2013, ApJ, 772, 134
Milisavljevic, D., & Fesen, R. A. 2017, in The Supernova—Supernova Remnant Connection, ed. A. W. Alsabti & P. Murdin (Cham: Springer), 2211
Milisavljevic, D., Fesen, R. A., Chevalier, R. A., et al. 2012, ApJ, 751, 25
Milisavljevic, D., Fesen, R. A., Kirshner, R. P., & Challis, P. 2009, ApJ, 692, 839
Milisavljevic, D., Fesen, R. A., Leibundgut, B., & Kirshner, R. P. 2008, ApJ, 684, 1170
Patnaude, D. J., Ellison, D. C., & Slane, P. 2009, ApJ, 696, 1956
Patnaude, D. J., Slane, P., Raymond, J. C., & Ellison, D. C. 2010, ApJ, 725, 1476
Porquet, D., Dubau, J., & Grosso, N. 2010, SSRv, 157, 103
Porquet, D., Mewe, R., Dubau, J., Raassen, A. J. J., & Kaastra, J. S. 2001, A&A, 376, 1113
Quirola-Vásquez, J., Bauer, F. E., Dwarkadas, V. V., et al. 2019, MNRAS, 490, 4536
Ramakrishnan, V., & Dwarkadas, V. V. 2020, ApJ, 901, 119
Sato, T., & Hughes, J. P. 2017, ApJ, 840, 112
Sato, T., Maeda, K., Nagataki, S., et al. 2021, Natur, 592, 537
van der Walt, S., Colbert, S. C., & Varoquaux, G. 2011, CSE, 13, 22
Verner, D. A., Ferland, G. J., Korista, K. T., & Yakovlev, D. G. 1996, ApJ, 465, 487
Vink, J. 2012, A&ARv, 20, 49
Wilms, J., Allen, A., & McCray, R. 2000, ApJ, 542, 914
Winkler, P. F., Coffin, S. C., Blair, W. P., Long, K. S., & Kuntz, K. D. 2021, ApJ, 908, 80
XRISM Science Team 2020, arXiv:2003.04962
Yamaguchi, H., Badenes, C., Petre, R., et al. 2014, ApJL, 785, L27